



Publication Year	2021
Acceptance in OA	2022-06-09T15:29:01Z
Title	Evidence for multiple Ferrel-like cells on Jupiter
Authors	Duer, Keren, Gavriel, Nimrod, Galanti, Eli, Kaspi, Yohai, Fletcher, Leigh N., Guillot, Tristan, Bolton, Scott J., Levin, Steven M., Atreya, Sushil K., GRASSI, Davide, Ingersoll, Andrew P., Li, Cheng, Li, Liming, Lunine, Jonathan I., Orton, Glenn S., Oyafuso, Fabiano A., Waite, J. Hunter
Publisher's version (DOI)	10.1029/2021GL095651
Handle	http://hdl.handle.net/20.500.12386/32260
Journal	GEOPHYSICAL RESEARCH LETTERS
Volume	48

Evidence for multiple Ferrel-like cells on Jupiter

Keren Duer^{*1}, Nimrod Gavriel^{*1}, Eli Galanti¹, Yohai Kaspi¹, Leigh N. Fletcher², Tristan Guillot³, Scott J. Bolton⁴, Steven M. Levin⁵, Sushil K. Atreya⁶, Davide Grassi⁷, Andrew P. Ingersoll⁸, Cheng Li⁶, Liming Li⁹, Jonathan I. Lunine¹⁰, Glenn S. Orton⁵, Fabiano A. Oyafuso⁵, J. Hunter Waite, Jr.⁴

¹Department of Earth and Planetary Sciences, Weizmann Institute of Science, Rehovot, Israel

²School of Physics and Astronomy, University of Leicester, University Road, Leicester, LE1 7RH, UK

³Université Côte d'Azur, OCA, Lagrange CNRS, 06304 Nice, France

⁴Southwest Research Institute, San Antonio, Texas, TX, USA

⁵Jet Propulsion Laboratory, California Institute of Technology, 4800 Oak Grove Drive, Pasadena, CA

91109, USA

⁶Department of Climate and Space Sciences and Engineering, University of Michigan, Ann Arbor, MI,

USA

⁷Istituto di Astrofisica e Planetologia Spaziali, INAF, Rome, Italy

⁸California Institute of Technology, Pasadena, California, USA

⁹University of Houston, Houston, TX, USA

¹⁰Department of Astronomy, Cornell University, Ithaca, New York 14853, USA

*These authors contributed equally to this work

Key Points:

- Measurements from multiple instruments of the Juno mission are interpreted to reveal the meridional circulation beneath Jupiter's clouds
- 16 Jet-paired deep cells, extending to at least 240 bar, are revealed between latitudes 60°S and 60°N, driven by turbulence similar to Earth's Ferrel cells
- The findings are supported by modeling the advection of tracers due to the cells, showing agreement with NH₃ data

Corresponding author: Keren Duer, keren.duer@weizmann.ac.il

Abstract

Jupiter’s atmosphere is dominated by multiple jet streams which are strongly tied to its 3D atmospheric circulation. Lacking a rigid bottom boundary, several models exist for how the meridional circulation extends into the planetary interior. Here we show, collecting evidence from multiple instruments of the Juno mission, the existence of mid-latitude meridional circulation cells which are driven by turbulence, similar to the Ferrel cells on Earth. Different than Earth, which contains only one such cell in each hemisphere, the larger, faster rotating Jupiter can incorporate multiple cells. The cells form regions of upwelling and downwelling, which we show are clearly evident in Juno’s microwave data between latitudes 60°S and 60°N. The existence of these cells is confirmed by reproducing the ammonia observations using a simplistic model. This study solves a long-standing puzzle regarding the nature of Jupiter’s sub-cloud dynamics and provides evidence for 8 cells in each Jovian hemisphere.

Plain Language Summary

The cloud layer of Jupiter is divided into dark and bright bands that are shaped by strong east-west winds. Such winds in planetary atmospheres are thought to be tied with a meridional circulation. The Juno mission collected measurements of Jupiter’s atmosphere at various wavelengths, which penetrate the cloud cover. Here we provide evidence, using the Juno data, of 8 deep Jovian circulation cells in each hemisphere encompassing the east-west winds, gaining energy from atmospheric waves, and extending at least to a depth of hundreds of kilometers. Different than Earth, which has only 1 analogous cell in each hemisphere, known as a Ferrel cell, Jupiter can contain more cells due to its larger size and faster spin. To support the presented evidence, we modeled how ammonia gas would spread under the influence of such cells and compared it to the Juno measurements. The presented results shed light on the unseen flow structure beneath Jupiter’s clouds.

1 Introduction

Over the last few decades, spacecraft and ground-based observations have gathered data about Jupiter’s atmosphere, including measurements of cloud reflectance (García-Melendo & Sánchez-Lavega, 2001), winds (Porco et al., 2003; Salyk et al., 2006; Tolleson et al., 2017), composition (Taylor et al., 2004) and lightning flashes (Little et al., 1999). Since 2016, the Juno spacecraft has provided unprecedented measurements that revealed new information on the deep dynamics of Jupiter (Bolton et al., 2017). Gravity science enabled an accurate mapping of Jupiter’s gravitational field (Iess et al., 2018), resulting in the inference that the zonal jets penetrate ~ 3000 km deep (Kaspi et al., 2018; Guillot et al., 2018), where they possibly decay due to magnetic drag (Liu et al., 2008; Dietrich & Jones, 2018; Kaspi et al., 2020) and may also require the presence of a stable layer (Christensen et al., 2020). The Jovian Infrared Auroral Mapper (JIRAM) provided measurements of tropospheric species distribution below the cloud level (Grassi et al., 2020). The Microwave Radiometer (MWR) measurements, inferred as brightness temperature (T_b), revealed the deep ammonia abundance (Li et al., 2017; Oyafuso et al., 2020), as well as lightning at a frequency of 600 MHz (Brown et al., 2018). The combination of these observations allows the essential nature of Jupiter’s deep overturning circulation to be revealed, as the flows associated with such circulation are directly related to cloud formation, temperature variations, lightning occurrences, tracer distributions and turbulence.

Earth’s atmosphere is commonly referred to as possessing a three-cell meridional structure in each hemisphere (Vallis, 2017), which can be recognized in the zonal-averaged velocities. Circulation cells of such nature are thought to prevail in the atmospheres of terrestrial planets (Read et al., 2018) and were observed, for example, on Mars (Lewis

et al., 2007) and Venus (Limaye, 2007). On the terrestrial planets, the solid surface drag plays a part in maintaining the circulation in the cells. However, as the giant planets hold no such surface, the mere possibility of them possessing meridional circulation cells remained uncertain. Earth’s midlatitudes are governed by the Ferrel cells, which are driven by atmospheric turbulence, creating regions of eddy momentum flux convergence at midlatitudes (Vallis, 2017). These cells accompany the midlatitude jets and are connected to the cloud structure in Earth’s atmosphere.

The prominent banded structure at the cloud tops of Jupiter’s atmosphere (Fig. 1a) has been observed for centuries (Vasavada & Showman, 2005). These reflectivity contrasts are partially aligned (mainly at low latitudes, Ingersoll et al. (2000)) with the belts and zones (Fig. 1a), defined by the sign of the zonal-wind vorticity ($\bar{\zeta} = -\partial\bar{u}/\partial y$ in Fig. 1c, where u is zonal velocity, y is in the meridional direction and an over-line represents a zonal mean). Voyager measurements suggested that the zones are associated with ascending motion, but this was limited to low latitudes due to its equatorial trajectory and to altitudes above 0.5 bar (Gierasch et al., 1986). The latitudinal profile of the zonal wind, calculated using cloud-tracking (Garcia-Melendo & Sánchez-Lavega, 2001; Porco et al., 2003; Tollefson et al., 2017), reveals that the equatorial region is characterized by a strong eastward flow, while the midlatitudes exhibit alternating jets, spaced $2\text{--}8^\circ$ apart in latitude (Fig. 1b). The midlatitude jets are correlated with the eddy momentum flux convergence (Salyk et al., 2006) ($-\partial(\overline{u'v'})/\partial y$ in Fig. 1d, where v is meridional velocity and an apostrophe represents deviations from the zonal mean, i.e. “eddy” terms), implying that the midlatitude jets are eddy-driven (Ingersoll et al., 2000; Young & Read, 2017), similar to the jets within Earth’s Ferrel cells (Schneider, 2006; Vallis, 2017). To illustrate the relation between the jets and the eddies, regions of positive (negative) vorticity gradient, $\partial\zeta/\partial y = -\partial^2\bar{u}/\partial y^2$, at midlatitudes, are marked by light red (blue) bands (Fig. 1), where counter-clockwise (clockwise) Ferrel-like circulation cells are expected in the northern hemisphere (NH). Similar circulations, but in opposite directions, apply for the southern hemisphere (SH). Evidence for vertical motion comes also from observations of lightning flashes (Little et al., 1999; Porco et al., 2003; Brown et al., 2018), suggesting updrafts in cyclonic belt regions (e.g., Fig. 1e).

Additional information regarding Jupiter’s deep atmosphere can be obtained by probing Jupiter’s interior at microwave frequencies. Juno’s MWR has 6 microwave channels (Janssen et al., 2017), each measuring the atmospheric T_b at a different depth (Janssen et al., 2017; Bolton et al., 2017; Oyafuso et al., 2020; Fletcher et al., 2021), and collectively covering the range between ~ 0.7 and ~ 240 bar (Fig. 1g,h, see also supporting information - SI). T_b measurements are affected by both ammonia abundance and temperature [and water in the case of the longest wavelengths, Li et al. (2017, 2020); Fletcher et al. (2021)]. If the latitudinal gradients of T_b were primarily driven by temperature changes, then thermal wind balance implies that the midlatitude jets strengthen from the cloud-deck to about ~ 8 bar, and then decay slowly towards the interior (Fletcher et al., 2021). However, interpreting T_b as temperature would also imply that the equatorial wind double its magnitude below the cloud level (Bolton et al., 2017), which is inconsistent with gravity constraints (Duer et al., 2020). Thus, the latitudinal variation of T_b is probably governed by ammonia opacity, resulting in a map of ammonia abundance (Li et al., 2017), and implying that the zonal winds are nearly barotropic (Fletcher et al., 2021). The overall ammonia structure, supported also by earlier observations (de Pater et al., 2001), reveals stratification of ammonia with depth, although the mean ammonia profile changes the sign of its vertical gradient at the $\sim 2\text{--}8$ bar region (Giles et al., 2017; Li et al., 2017; de Pater et al., 2019). The atmospheric depletion and stratification of ammonia is likely linked to small-scale storm activity (Guillot, Li, et al., 2020; Guillot, Stevenson, et al., 2020), where water-ammonia hail, forming around the 1-bar level, falls below the water-cloud base and releases ammonia and water at altitudes below 10 bar (Guillot, Stevenson, et al., 2020). Additional measurements of ammonia come from Juno’s JIRAM, which evaluated the ammonia distribution at a depth of $\sim 5\text{--}6$ bar (Grassi et al., 2010, 2020)

(Fig. 1f), indicating, as the MWR measurements, that ammonia varies with latitude. These variations are the key observation for this study, as ammonia anomalies (deviations from the isobaric mean) can reveal details about Jupiter’s overturning circulation (Ingersoll et al., 2017; Fletcher et al., 2021; Lee & Kaspi, 2021).

2 Ammonia anomalies due to vertical advection

In the presence of a stable vertical ammonia concentration gradient, advection by the vertical branches of a meridional circulation can affect the concentration distribution, potentially leading to steady anomalies. Therefore, the wavy structure of Jupiter’s ammonia distribution (Fig. 1f-h) can be explained by the presence of meridional circulation cells. On Jupiter, as condensation of ammonia is expected only at the upper levels of the atmosphere (0.5 – 1 bar), the ammonia concentration at those levels should be lower than at depth (Fletcher et al., 2020). In addition, precipitation, small-scale turbulence, thermochemical and chemical reactions, and diffusion are also expected to determine the vertical ammonia distribution (M_a) (Guillot, Stevenson, et al., 2020). The M_a profile estimated from the MWR (Li et al., 2017) reveals a local minimum at ~ 6 bar (Fig. 2a). This profile is used in this study as the background state, to explain the ammonia anomalies.

Here, we focus on two regions with distinctly different deep dynamics: the equatorial region (planetocentric latitudes 20°S to 20°N), where superrotation is assumed to be fueled by eddy momentum fluxes perpendicular to the spin axis (e.g., Busse, 2002), and midlatitudes (60°S to 20°S and 20°N to 60°N), where alternating jets are postulated to be driven by horizontal eddies associated with mass-transporting meridional cells (e.g., Salyk et al., 2006; Schneider & Liu, 2009; Young et al., 2019).

We begin with the midlatitudes, where the meridional cells are mechanically driven (see below) by turbulence, similar to Earth’s Ferrel cells, which form as a consequence of atmospheric waves breaking in midlatitudes (Vallis, 2017). Unlike the largely baroclinic midlatitudes of Earth, which result in mostly non-mass-transporting Ferrel cells (Jukes, 2001; Vallis, 2017), the predominantly barotropic flows on Jupiter (at the depth range associated with the MWR measurements) (Kaspi et al., 2018; Kaspi et al., 2020; Galanti & Kaspi, 2021) may allow mass-transporting meridional cells (see SI). Consistently, deep convection models of Jupiter also show barotropic flows (e.g., Busse, 1976; Aurnou & Olson, 2001). The upper branch of Earth’s Ferrel cells consists of a balance between the Coriolis force and the eddy momentum flux convergence,

$$-f\bar{v} = -\frac{\partial(\overline{u'v'})}{\partial y}, \quad (1)$$

where f is the Coriolis parameter. This upper branch balance, which is the leading order balance of the steady state zonal mean zonal momentum equation, is expected to hold within the equivalent cells on Jupiter (see SI). This balance can hold down to a depth of only a few bars, as inferred from energy considerations (Liu & Schneider, 2010), implying flows from belts to zones within the cloud layer of the Jovian atmosphere. In the lower branch of the terrestrial Ferrel cells, the balance is between the Coriolis force and a surface drag (Vallis, 2017). Since the Jovian atmosphere lacks a bottom solid boundary, surface drag cannot act to oppose the Coriolis force, although it has been suggested that if the cells extend as deep as the jets (Kaspi et al., 2020), the Lorentz force can act as a magnetic drag (Liu et al., 2008; Liu & Schneider, 2010; Wicht et al., 2019). Another possible mechanism that allows the jets to be barotropic in the upper atmosphere and decay in the interior is the presence of a stable layer, as was shown lately in several studies (Debras & Chabrier, 2019; Christensen et al., 2020; Wicht & Gastine, 2020).

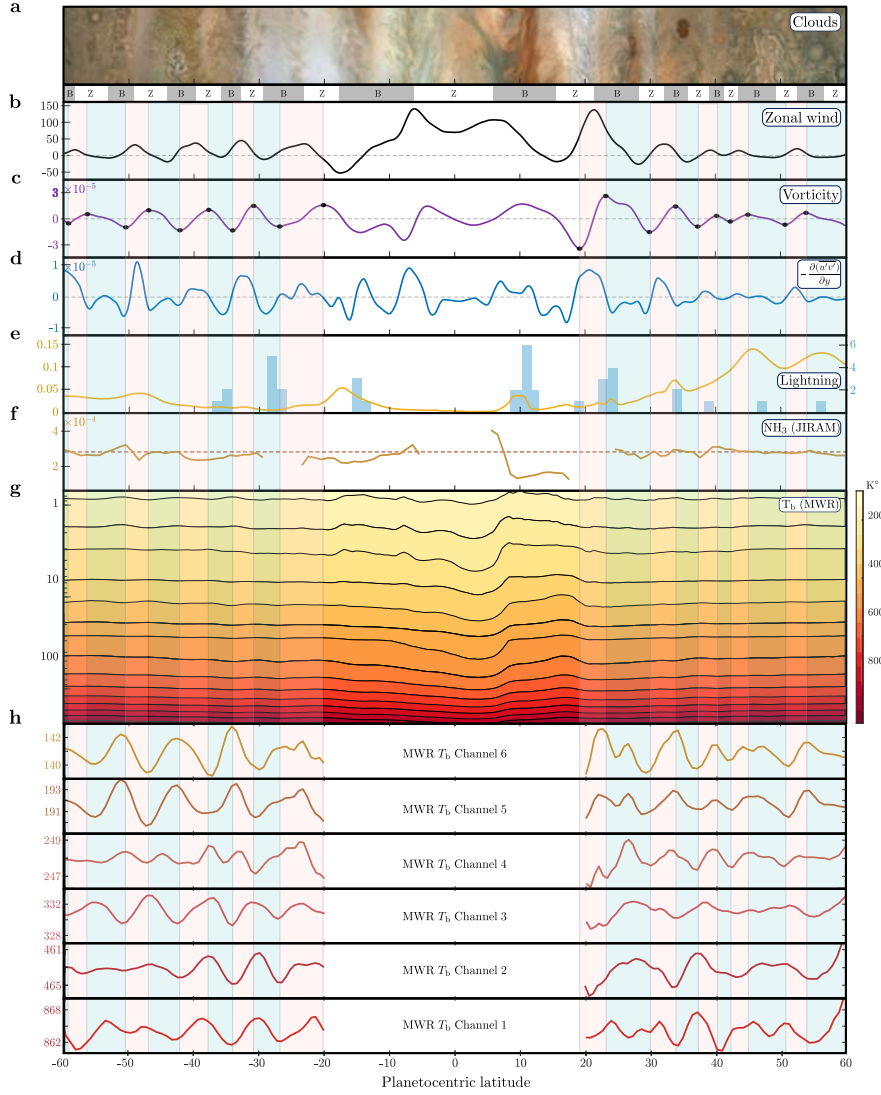


Figure 1: Observations of Jupiter’s atmosphere. (a) Image of Jupiter’s clouds (longitudes $69 - 87^\circ$) taken by JunoCam on Dec. 26th 2019 during perijove 24 (image credit: NASA/JPL/SwRI/MSSS/Gerald Eichstaedt/John Rogers), with the traditional “dark” belts (“bright” zones) defined as regions of cyclonic (anticyclonic) vorticity, identified below as ‘B’ (‘Z’). (b) Jupiter’s zonally averaged zonal wind [$\pm 15 \text{ m s}^{-1}$] measured by the Hubble space telescope on December 11, 2016, during Juno’s third perijove (Tollefson et al., 2017). (c) The zonally averaged vorticity [s^{-1}], calculated from the zonal wind profile (panel b). Black dots represent local extrema in the midlatitudes. (d) Eddy momentum flux convergence [$\pm 2 \times 10^{-6} \text{ m s}^{-2}$] calculated from 58 image pairs taken by Cassini during its Jupiter flyby in December, 2000 (Salyk et al., 2006). (e) Lightning detections [s^{-1}] by Juno’s MWR during perijoves 1-8 (yellow, left axis, Brown et al., 2018) and number of lightning storms detected by the Cassini during its flyby (blue, right axis, Porco et al., 2003). (f) Distribution of ammonia [volume mixing ratio] and its mean (dashed) at a depth of ~ 6 bar, measured by Juno’s JIRAM during perijoves 1-15 (Grassi et al., 2020). (g) Nadir T_b [$^\circ\text{K}$] (color) interpolated between pressure levels of 0.7 and 240 bar (vertical axis), measured by Juno’s MWR during perijoves 1-12 (Oyafuso et al., 2020). (h) Reconstructed MWR Brightness temperature at midlatitudes. A frequency filter is applied according to Eq. S7. The standard deviation of each channel and latitude is available in Fig. S3 and Fig. S4. It can be seen that T_b changes its trend at the borders between cells, consistent with the Ferrel-like cells hypothesis. (b-h) Light red (blue) bands in the midlatitudes indicate regions of positive (negative) vorticity gradients.

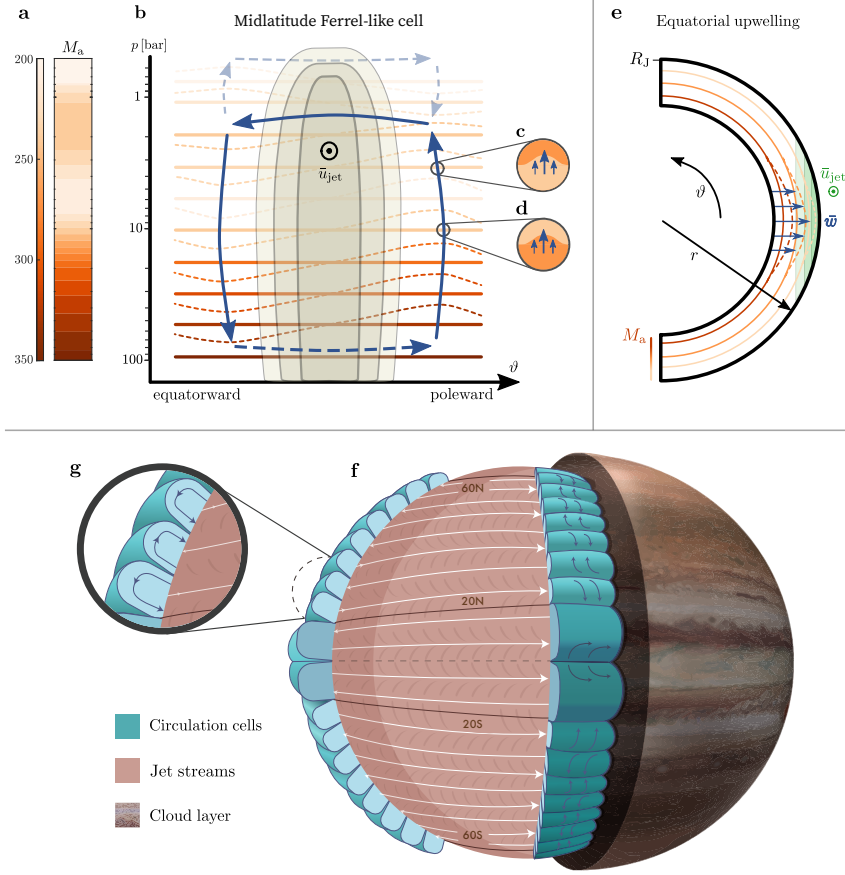


Figure 2: Schematics of Jupiter’s meridional circulation as inferred from the ammonia distribution. (a) The vertical structure of the meridionally averaged ammonia concentration (M_a) [ppm], as interpreted from the T_b data (Li et al., 2017). (b) Illustration of a midlatitude Ferrel-like circulation cell (blue arrows) in the NH, looking from east towards the west. The cells are accompanied by an eddy-driven barotropic jet (\bar{u}), which peaks at the center of the cell (beige contours). Ammonia constant-concentration lines are illustrated with orange shades (according to the ammonia vertical profile from panel a). Dashed orange lines are deviations from M_a , driven by vertical advection. The return flow of the cell, illustrated by a dashed blue arrow, lies at an unknown depth. An oppositely directed upper cell, as suggested by pre-Juno measurements (Ingersoll et al., 2000; Showman & de Pater, 2005; Fletcher et al., 2020), is demonstrated by dashed transparent arrows. p is pressure, taken as a vertical coordinate. (c) A closer look at the region where the rising air advects ammonia-poor fluid to an ammonia-rich layer, associated with pressure levels between 1.5 and 6 bar. (d) Here, rising gas drags higher ammonia concentration to a lower ammonia concentration region, associated with pressure levels deeper than 6 bar. (e) A cross section of Jupiter’s equatorial upwelling (\bar{w}), associated with a superrotating jet (\bar{u} , green contours), leading to ammonia concentration maximum. The equatorial M_a (orange contours) is assumed to decrease with radius (Fig. S8). R_J is Jupiter’s radius and ϑ and r are the latitudinal and radial directions, respectively. (f) A figurative cross section of Jupiter’s meridional circulation and (g) a magnification of the midlatitude circulation cells. The circulation cells (blue) are axisymmetric in the zonal direction. The pink shell represents a deep layer characteristic for all depths within the circulation cells. The white arrows represent alternating jet streams and are symmetric around the equator for the purpose of clarity. Each jet between latitudes $20^\circ - 60^\circ$ S/N is accompanied by a turbulence-driven circulation cell (blue arrows) in the meridional plane as illustrated in panel b. The equatorial upwelling associated with the superrotating jet is drawn at the equator, as illustrated in panel e, as part of a larger possible equatorial cell (dark blue).

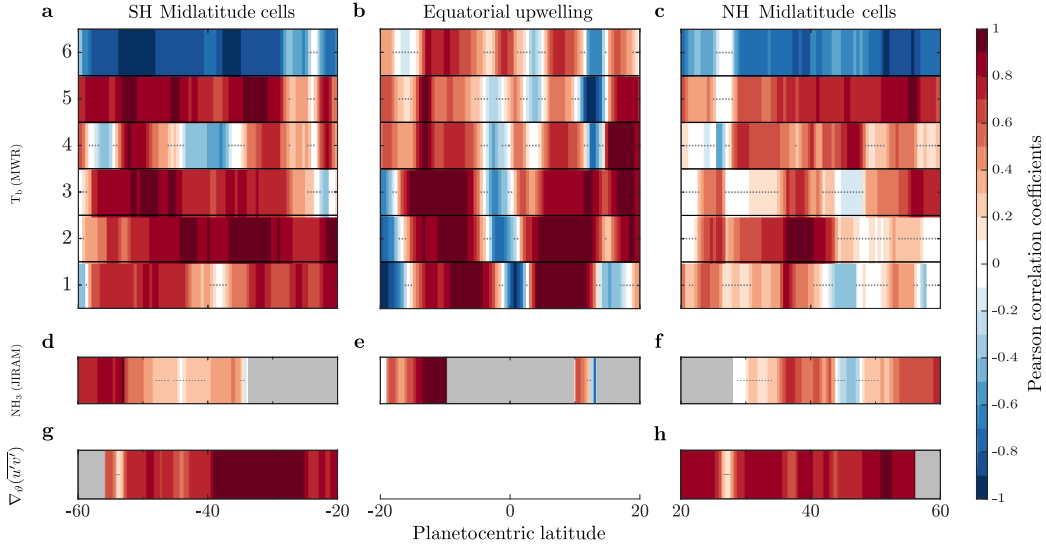


Figure 3: Pearson correlation coefficients as a function of latitude. The correlations exemplify the relations presented in Fig. 2. (a) and (c), correlations calculated between the zonal jets (\bar{u}) and the T_b meridional gradients ($\partial_y T_b$), adjusted by the sign of the vertical gradient of M_a , in the six MWR channels, for the SH and NH, respectively. (b) Correlations computed between the zonal jet velocity and T_b ($\bar{u} \propto -T_b$). (d) and (f), Correlations between the zonal velocity and the ammonia abundance gradients ($\partial_y \text{NH}_3$), measured by JIRAM, in the SH and NH, respectively. (e) Correlations between the zonal velocity and the ammonia abundance from JIRAM ($\bar{u} \propto \text{NH}_3$). (g) and (h) Correlations between the zonal velocity and the eddy momentum flux convergence ($\bar{u} \propto -\partial_y (\overline{u'v'})$), in the SH and NH, respectively. Gray dots represent correlations that are not statistically significant (confidence level 95%) and gray regions show where measurements were not available. No data is available for the eddy fluxes in the equatorial region, as evaluating them requires measurements of the vertical winds (see SI), which are yet to be achieved.

178 The direction of each Ferrel-like cell corresponds to the direction of the respective
 179 midlatitude jet. Eastward (westward) jets are located in cells of eastward momentum
 180 flux convergence (divergence) implying (Eq. 1) a counterclockwise (clockwise) circula-
 181 tion in the NH, and a clockwise (counterclockwise) circulation in the SH (Fig. 1b,d). The
 182 upper branch of the Ferrel-like cells may coincide with the lower branch of stacked up-
 183 per cells with an opposite circulation (Ingersoll et al., 2000; Showman & de Pater, 2005)
 184 (dashed transparent lines in Fig. 2b), and therefore may share the same balance (Eq. 1).
 185 Indications for the upper cells come from temperature and shallow tracer distributions
 186 (Gierasch et al., 1986; Fletcher et al., 2016; de Pater et al., 2019). Similar to the balance
 187 describing the deeper branch of the lower cells, the upper branch of the upper cells re-
 188 quires a drag force, which may result from breaking of atmospheric waves (Gierasch et
 189 al., 1986; Ingersoll et al., 2021).

190 The background ammonia profile is skewed by the vertical branches of the cells (dashed
 191 orange lines in Fig. 2b), maximizing the ammonia meridional gradient where the jet ve-
 192 locity peaks (i.e., in the middle of the cell). This means that a correlation (along isobars)
 193 is expected between the zonal jets and the meridional gradient of the ammonia concen-
 194 tration at midlatitudes (Duer et al., 2020; Fletcher et al., 2021). However, since the ver-
 195 tical gradient of M_a changes with depth (Li et al., 2017) (Fig. 2a), the nature of the cor-
 196 relation should change as well, as illustrated in Fig. 2c,d. These simple considerations

197 motivate the examination of the correlation between \bar{u} and $\partial_y m_a$ ($-\partial_y T_b$) in midlati-
 198 tudes (Fig. 3a,c, also see SI). Note that T_b corresponds inversely to ammonia abundance
 199 at a certain pressure level (Li et al., 2017). For a deep-wind estimate, we use the mea-
 200 sured cloud-level winds (Tollefson et al., 2017) projected inward in a direction parallel
 201 to the axis of rotation, without any change in magnitude (in the upper 240 bar), as im-
 202 plied by gravity measurement constraints (Galanti & Kaspi, 2021; Galanti et al., 2021).
 203 The correlations are performed using a 4° latitudinal bin (see SI). By this, the suggested
 204 correlations in Fig. 2 can be tested locally, rather than over an entire hemisphere (Duer
 205 et al., 2020; Fletcher et al., 2021).

206 At midlatitudes the overall positive correlations for MWR channels 1-5 indicate the
 207 existence of Ferrel-like cells at depths between 1.5 and 240 bar (Fig. 3a,c). The positive
 208 correlation with ammonia estimates by JIRAM (Fig. 3d,f) further strengthens the promi-
 209 nence of the proposed cells. Channel 6 (~ 0.7 bar) exhibits negative correlations in mid-
 210 latitudes (Fig. 3a,c), implying that the deep cells do not extend higher than ~ 1 bar,
 211 and support the existence of counter-rotating cells above that level (Ingersoll et al., 2000;
 212 Showman & de Pater, 2005; Fletcher et al., 2020). To verify that the relation shown in
 213 Eq. 1 holds in the cells as illustrated in Fig. 2b, regional correlations between \bar{u} and $-\partial_y \left(\overline{u'v'} \right)$
 214 are shown for midlatitudes (Fig. 3g,h). This positive correlation further strengthens the
 215 existence of the Ferrel-like cells, where converging eddy momentum fluxes are the source
 216 of momentum. Overall, the correlation analysis reveals multiple deep Ferrel-like cells,
 217 extending from ~ 1 bar to at least 240 bar.

218 The equatorial region of Jupiter, characterized by a wide eastward jet, needs to be
 219 treated differently. Gravity analysis reveals that Jupiter’s interior (deeper than ~ 3000 km)
 220 is rotating as a rigid body (Guillot et al., 2018). Extending the zonal wind along the di-
 221 rection of the spin axis thus separates the equatorial region (17° S to 17° N) from the trun-
 222 cated cells at midlatitudes (see SI). The superrotating wind at low latitudes requires a
 223 source of momentum (Imamura et al., 2020). Theories for such sources include merid-
 224 ional (Potter et al., 2014; Laraia & Schneider, 2015) and vertical (Aurnou & Olson, 2001;
 225 Busse, 2002; Christensen, 2002; Heimpel et al., 2005; Kaspi et al., 2009; Dietrich & Jones,
 226 2018), propagation of waves. For the vertical case, several studies have shown that an
 227 equatorial superrotation in giant planets can be driven by eddy momentum fluxes per-
 228 pendicular to the axis of rotation (Heimpel et al., 2005; Kaspi et al., 2009; Gastine et
 229 al., 2014). These fluxes transfer momentum outwards and lead to a mean upwelling at
 230 the equatorial region (see SI). Such an upwelling should lead to a maximum concentra-
 231 tion anomaly of any stably stratified matter (Fig. 2e). In the equatorial region, the min-
 232 imum in M_a around ~ 6 bar nearly vanishes (Fig. S8), suggesting that the positive am-
 233 monia anomalies at the equatorial region (Fig. S2a) are due to the upwelling from deep.
 234 To examine this, at the equator, the correlation is calculated between the zonal veloc-
 235 ity (\bar{u}) and the ammonia concentration itself ($-T_b$ for the MWR or NH_3 for the JIRAM
 236 measurements). Using a regional correlation analysis (see SI), it is apparent that the cor-
 237 relations are largely positive at all depths (Fig. 3b,e), implying that an equatorial up-
 238 welling is dominant from the cloud deck and down to at least 240 bar. Very close to the
 239 equator, the correlation is negative due to the local minimum in the zonal velocity (Fig. 1b).

240 3 Model reconstruction of Jupiter’s ammonia distribution

241 To further validate that the positive correlations shown in Fig. 3a,c are indeed due
 242 to the existence of meridional circulation cells, we reconstruct the measured variations
 243 using a simplified advection-relaxation model. Beginning with a steady-state zonal-mean
 244 conservation of species equation for ammonia, assuming that diffusion terms are small,
 245 the leading-order balance is

$$\bar{w}(\vartheta, r) \frac{\partial m_a(\vartheta, r)}{\partial r} + \bar{v}(\vartheta, r) \frac{\partial m_a(\vartheta, r)}{r \partial \vartheta} = -G(r) (m_a(\vartheta, r) - M_a(r)), \quad (2)$$

246 where \bar{w} is the zonally averaged radial velocity, and m_a , the variable solved for by the
 247 model, is the (zonal-mean) molar fraction of ammonia. M_a is the ammonia concentra-
 248 tion averaged over isobaric surfaces (Fig. 2a), and G is the inverse of a Newtonian re-
 249 laxation timescale. The two terms on the left-hand side represent advection by the mean
 250 circulation, and the right-hand side term is a source term parameterized as a simple New-
 251 tonian relaxation of ammonia. This relaxation term is assumed to include all the pro-
 252 cesses resulting in the observed M_a as it acts against local anomalies toward this mean
 253 vertical structure. To qualitatively illustrate how the Ferrel-like cells' footprint might
 254 appear in the ammonia distribution map (m_a), we solve the advection-relaxation bal-
 255 ance shown in Eq. 2, for the midlatitudes between 1.5 and 240 bar (see SI). As the bal-
 256 ance in Eq. 2 indicates, it is assumed that the relaxation time scale (G^{-1}) is such that
 257 the advection and relaxation terms balance each other.

258 The zonally averaged velocity components (\bar{v}, \bar{w}) of the circulation cells, necessary
 259 for setting the advection terms of Eq. 2, can be projected from the available wind data
 260 according to the outline illustrated in Fig. 2b. Specifically, we relate between the circula-
 261 tion cells and the wind data corresponding to the following assumptions (see also SI).
 262 The borders between the cells are set at local extrema of the observed cloud-level vorticity,
 263 the directions of the circulation cells are set according to the directions of the jets
 264 in the middle of each cell, and the strength of the circulation in each cell is set by the
 265 measured eddy momentum flux convergence along the cell (Fig. S5). As the three terms
 266 in Eq. 2 should be proportional, but cannot be uniquely determined, the values of \bar{w} , \bar{v}
 267 and G are normalized (Fig. 4a). This normalization means that while the model can-
 268 not produce absolute values of winds due to unmeasured quantities, it can predict qual-
 269 itatively how these velocities would be structured spatially and what should be their rel-
 270 ative magnitudes, which are sufficient for assessing the existence of the cells. Using scal-
 271 ing arguments, the value of Jupiter's static stability has recently been estimated to be
 272 in the order of 10^{-2} s^{-1} (Lee & Kaspi, 2021), which can provide a further step towards
 273 estimating the magnitude of the velocities in the cells.

274 The described wind scheme results in upwellings (downwellings) on the poleward
 275 (equatorward) sides of eastward jets (Fig. 4a). The cells are reversed for westward jets.
 276 Finally, as a benchmark for the model results, derivation of the ammonia abundance ($m_a^{(\text{data})}$)
 277 from the measured T_b between the latitudes 60°S and 60°N is implemented (see SI, Fig. S2).
 278 As the depth of the cells, the width of their branches and the parameter G are unknown,
 279 an optimization procedure is performed for determining these parameters to best match
 280 the data (see SI). To ensure that this procedure does not influence the qualitative na-
 281 ture of the results, Eq. 2 is also solved with a predefined physically-oriented set of pa-
 282 rameters (Figs. S6 and S7).

283 Using the above assumptions, we solve Eq. 2 to predict the ammonia map ($m_a^{(\text{model})}$),
 284 and compare it to $m_a^{(\text{data})}$ (Fig. 4). We stress that the latitudinal variations appearing
 285 in the results (Fig. 4c), stem only from the cloud-level wind observations without any
 286 assumption on the meridional ammonia variation. For a clear comparison between the
 287 $m_a^{(\text{data})}$ and $m_a^{(\text{model})}$, M_a is subtracted from both, such that only anomalies are visible
 288 (Fig. 4b,c). Around 10 bar (Fig. 4b), where M_a greatly increases with depth, enriched
 289 (depleted) ammonia anomalies appear where upwellings (downwellings) are expected (Fig. 4a).
 290 These features flip sign around the 6-bar level, where M_a decreases with depth. These
 291 elements are captured well by the advection-relaxation model (Fig. 4c). In the SH, all
 292 18 anomalies apparent in the observations have a counterpart of similar sign, shape and
 293 position in the model results, suggesting the existence of 8 meridional circulation cells.
 294 This agreement validates that advection by the vertical branches of the cells is the main
 295 contributor in the creation of the observed ammonia anomalies. In the NH, similar re-
 296 sults are achieved, although the cells are slightly less coherent, perhaps due to unexplained

297 differences between the perijoves in the NH midlatitudes [Fig. S3, Oyafuso et al. (2020);
 298 Fletcher et al. (2021)], which might mask the cells' footprints in the MWR data. Nev-
 299 ertheless, the lightning data reinforces the existence of the NH cells, as lightning peaks
 300 are aligned with the rising branch of the cells at the poleward side of the eastward jets
 301 (Fig. 1e, Fig. S1), which combined with the MWR data (Fig. 4b-d) provide indication
 302 for 8 northern cells. Additional NH centered perijoves during the Juno extended mis-
 303 sion may provide data to better constrain the NH cells. For more intuition, one can look
 304 at the full ammonia map (Fig. 4d), where iso-concentration lines are pulled up and down
 305 by the vertical winds (as schematically illustrated in Fig. 2b), emphasizing the locations
 306 of the 16 eddy-driven cells evident in the MWR data.

307 4 Discussion

308 The identified array of alternating cells in midlatitudes, along with the equatorial
 309 upwelling, are key features in the meridional overturning circulation of the Jovian at-
 310 mosphere (Fig. 2f). The cell's depth that can be inferred from the MWR measurements
 311 is limited to the sensing range (~ 240 bar), and while the midlatitudinal cells are me-
 312 chanically driven, as the Ferrel cells in Earth's troposphere, they are likely to extend deeper
 313 into the planet, as suggested by multiple theoretical studies (e.g., Liu & Schneider, 2010;
 314 Christensen et al., 2020). Similarly, deep meridional cells, which are mechanically driven,
 315 have been suggested to exist on the Sun (Miesch & Hindman, 2011).

316 This study provides an explanation for the observed meridional ammonia anom-
 317 alies, given the meridionally averaged vertical ammonia profile. The consistency of these
 318 results suggest that the T_b latitudinal variations are dominated by the opacity of a pas-
 319 sive tracer, rather than the kinetic temperature. Note that evidence for the part of the
 320 deep cells extending from 1.5 to 6 bar depends on the flip of the background ammonia
 321 gradient (Fig. 2a), and without it these depths might be part of upper inverse cells (Fletcher
 322 et al., 2021). The shape of this vertical profile might be set by precipitation, diffusion,
 323 and small-scale mixing, all of which might change with latitude and depth (Guillot, Li,
 324 et al., 2020). Nonetheless, the remarkable agreement between the model and the data,
 325 together with the robust correlation analysis, provide strong evidence that the observed
 326 distribution of ammonia is governed by the existence, number, position and relative strength
 327 of the Ferrel-like circulation cells in Jupiter.

328 Acknowledgments

329 All the data used in this study is publicly available, see Tollefson et al. (2017) for the
 330 winds data, Salyk et al. (2006) for the eddies data, Li et al. (2017) for the ammonia data,
 331 Brown et al. (2018) for the lightning data and Oyafuso et al. (2020) for the brightness
 332 temperature data.

333 References

- 334 Aurnou, J. M., & Olson, P. L. (2001). Strong zonal winds from thermal convection in
 335 a rotating spherical shell. *Geophys. Res. Lett.*, *28*(13), 2557-2559.
- 336 Bolton, S. J., Adriani, A., Adumitroaie, V., Allison, M., Anderson, J., Atreya, S., ...
 337 Wilson, R. (2017, May). Jupiter's interior and deep atmosphere: The initial
 338 pole-to-pole passes with the Juno spacecraft. *Science*, *356*, 821-825.
- 339 Brown, S., Janssen, M., Adumitroaie, V., Atreya, S., Bolton, S., Gulkis, S., ... Con-
 340 nerney, J. (2018). Prevalent lightning sferics at 600 megahertz near Jupiter's
 341 poles. *Nature*, *558*(7708), 87-90.
- 342 Busse, F. H. (1976). A simple model of convection in the Jovian atmosphere. *Icarus*,
 343 *29*, 255-260.
- 344 Busse, F. H. (2002, April). Convective flows in rapidly rotating spheres and their dy-

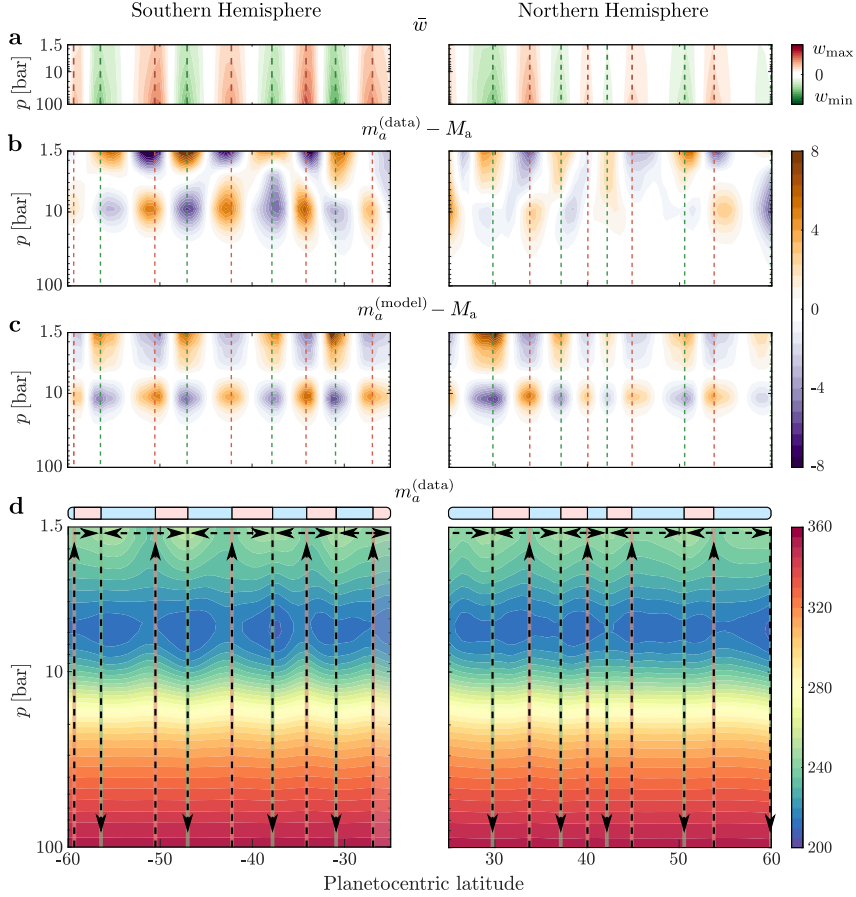


Figure 4: Jupiter’s Ammonia distribution driven by an array of circulation cells. (a) The normalized vertical zonal-mean wind (\bar{w}), as a function of latitude and pressure, used in the model. Red and green contours are upward and downward winds, respectively. (b) The ammonia anomalies reconstructed from the data [ppm]. Here the vertical mean profile M_a is removed from the ammonia map m_a . (c) The ammonia anomalies [ppm] produced by the advection-relaxation model. (d) The full reconstructed ammonia map $m_a^{(\text{data})}$ [ppm]. Arrows represent the direction of the cells’ vertical and meridional winds. (a-d) Red and green vertical lines are the locations of the upward and downward branches of the cells, respectively. For reference, light red (blue) bands indicate regions of positive (negative) vorticity gradient as in Fig. 1. The vertical axis is truncated at 100 bar as M_a becomes largely uniform beyond this depth, thereby suppressing footprints of advection.

- 345 namo action. *Phys. of Fluids.*, *14*, 1301-1314.
- 346 Christensen, U. R. (2002). Zonal flow driven by strongly supercritical convection in
347 rotating spherical shells. *J. Comp. Phys.*, *470*, 115-133.
- 348 Christensen, U. R., Wicht, J., & Dietrich, W. (2020). Mechanisms for limiting the
349 depth of zonal winds in the gas giant planets. *Astrophys. J.*, *890*(1), 61.
- 350 de Pater, I., Dunn, D., Romani, P., & Zahnle, K. (2001, January). Reconciling
351 Galileo Probe Data and Ground-Based Radio Observations of Ammonia on
352 Jupiter. *Icarus*, *149*(1), 66-78. doi: 10.1006/icar.2000.6527
- 353 Debras, F., & Chabrier, G. (2019). New models of Jupiter in the context of Juno
354 and Galileo. *Astrophys. J.*, *872*(1), 100.
- 355 de Pater, I., Sault, R. J., Wong, M. H., Fletcher, L. N., DeBoer, D., & Butler, B.
356 (2019). Jupiter's ammonia distribution derived from VLA maps at 3-37 GHz.
357 *Icarus*, *322*, 168-191.
- 358 Dietrich, W., & Jones, C. A. (2018, May). Anelastic spherical dynamos with radially
359 variable electrical conductivity. *Icarus*, *305*, 15-32.
- 360 Duer, K., Galanti, E., & Kaspi, Y. (2020). The range of Jupiter's flow structures
361 that fit the Juno asymmetric gravity measurements. *J. Geophys. Res. (Plan-*
362 *ets)*, *125*(8).
- 363 Fletcher, L. N., Greathouse, T. K., Orton, G. S., Sinclair, J. A., Giles, R. S., Irwin,
364 P. G., & Encrenaz, T. (2016). Mid-infrared mapping of Jupiter's temperatures,
365 aerosol opacity and chemical distributions with IRTF/TEXES. *Icarus*, *278*,
366 128-161.
- 367 Fletcher, L. N., Kaspi, Y., Guillot, T., & Showman, A. P. (2020). How well do we
368 understand the belt/zone circulation of Giant Planet atmospheres? *Space Sci.*
369 *Rev.*, *216*(2), 1-33.
- 370 Fletcher, L. N., Oyafuso, F. A., Allison, M., Ingersoll, A., Li, L., Kaspi, Y., ...
371 Bolton, S. (2021). Jupiter's temperate belt/zone contrasts revealed at depth
372 by Juno microwave observations. *Earth and Space Science Open Archive*, *35*.
373 doi: 10.1002/essoar.10506297.1
- 374 Galanti, E., & Kaspi, Y. (2021). Combined magnetic and gravity measurements
375 probe the deep zonal flows of the gas giants. *Mon. Not. Roy. Astro. Soc.*,
376 *501*(2), 2352-2362.
- 377 Galanti, E., Kaspi, Y., Duer, K., Fletcher, L. N., Ingersoll, A., Cheng, L., ... J.,
378 B. S. (2021). Constraints on the latitudinal profile of Jupiter's deep jets.
379 *Geophys. Res. Lett.*, *48*(9), e2021GL092912.
- 380 Garcia-Melendo, E., & Sánchez-Lavega, A. (2001). A study of the stability of jovian
381 zonal winds from HST images: 1995-2000. *Icarus*, *152*(2), 316-330.
- 382 Gastine, T., Wicht, J., Duarte, L. D. V., Heimpel, M., & Becker, A. (2014, August).
383 Explaining Jupiter's magnetic field and equatorial jet dynamics. *Geophys. Res.*
384 *Lett.*, *41*, 5410-5419.
- 385 Gierasch, P. J., Magalhaes, J. A., & Conrath, B. J. (1986, September). Zonal mean
386 properties of Jupiter's upper troposphere from Voyager infrared observations.
387 *Icarus*, *67*, 456-483.
- 388 Giles, R. S., Fletcher, L. N., Irwin, P. G., Orton, G. S., & Sinclair, J. A. (2017).
389 Ammonia in Jupiter's troposphere from high-resolution 5 μm spectroscopy.
390 *Geophys. Res. Lett.*, *44*(21), 10-838.
- 391 Grassi, D., Adriani, A., Moriconi, M. L., Ignatiev, N. I., D'Aversa, E., Colosimo, F.,
392 ... Iccioni, G. (2010). Jupiter's hot spots: Quantitative assessment of the re-
393 trieval capabilities of future IR spectro-imagers. *Planetary and Space Science*,
394 *58*(10), 1265-1278.
- 395 Grassi, D., Adriani, A., Mura, A., Atreya, S. K., Fletcher, L. N., Lunine, J. I., ...
396 Turrini, D. (2020). On the spatial distribution of minor species in Jupiter's
397 troposphere as inferred from Juno JIRAM data. *J. Geophys. Res. (Planets)*,
398 *125*(4).
- 399 Guillot, T., Li, C., Bolton, S. J., Brown, S. T., Ingersoll, A. P., Janssen, M. A., ...

- 400 Stevenson, D. J. (2020). Storms and the depletion of ammonia in Jupiter:
 401 ii. explaining the Juno observations. *J. Geophys. Res. (Planets)*, *125*(8),
 402 e2020JE006404.
- 403 Guillot, T., Miguel, Y., Militzer, B., Hubbard, W. B., Kaspi, Y., Galanti, E., ...
 404 Bolton, S. J. (2018). A suppression of differential rotation in Jupiter's deep
 405 interior. *Nature*, *555*, 227-230.
- 406 Guillot, T., Stevenson, D. J., Atreya, S. K., Bolton, S. J., & Becker, H. N. (2020).
 407 Storms and the depletion of ammonia in Jupiter: I. microphysics of mushballs.
 408 *J. Geophys. Res. (Planets)*, *125*(8), e2020JE006403.
- 409 Heimpel, M., Aurnou, J., & Wicht, J. (2005, Nov). Simulation of equatorial and
 410 high-latitude jets on Jupiter in a deep convection model. *Nature*, *438*, 193-
 411 196.
- 412 Iess, L., Folkner, W. M., Durante, D., Parisi, M., Kaspi, Y., Galanti, E., ... Bolton,
 413 S. J. (2018). Measurement of Jupiter's asymmetric gravity field. *Nature*,
 414 *555*(7695), 220-222.
- 415 Imamura, T., Mitchell, J., Lebonnois, S., Kaspi, Y., Showman, A. P., & Korablev,
 416 O. (2020). Superrotation in planetary atmospheres. *Space Sci. Rev.*, *216*(5),
 417 1-41.
- 418 Ingersoll, A. P., Adumitroaie, V., Allison, M. D., Atreya, S., Bellotti, A. A., Bolton,
 419 S. J., ... Steffes, P. G. (2017). Implications of the ammonia distribution on
 420 Jupiter from 1 to 100 bars as measured by the Juno microwave radiometer.
 421 *Geophys. Res. Lett.*, *44*(15), 7676-7685.
- 422 Ingersoll, A. P., Atreya, S., Bolton, S. J., Brueschaber, S., Fletcher, L. N., Galanti,
 423 E., ... Waite, H. (2021). Jupiter's overturning circulation: Breaking waves
 424 take the place of solid boundaries. *Geophys. Res. Lett.* (in review)
- 425 Ingersoll, A. P., Gierasch, P. J., Banfield, D., Vasavada, A. R., & Galileo Imaging
 426 Team. (2000, February). Moist convection as an energy source for the large-
 427 scale motions in Jupiter's atmosphere. *Nature*, *403*, 630-632.
- 428 Janssen, M. A., Oswald, J. E., Brown, S. T., Gulkis, S., Levin, S. M., Bolton,
 429 S. J., ... Wang, C. C. (2017, November). MWR: Microwave Radiometer
 430 for the Juno Mission to Jupiter. *Space Sci. Rev.*, *213*(1-4), 139-185. doi:
 431 10.1007/s11214-017-0349-5
- 432 Jukes, M. (2001). A generalization of the transformed Eulerian-mean meridional
 433 circulation. *Q. J. R. Meteorol. Soc.*, *127*(571), 147-160.
- 434 Kaspi, Y., Flierl, G. R., & Showman, A. P. (2009). The deep wind structure of the
 435 giant planets: Results from an anelastic general circulation model. *Icarus*, *202*,
 436 525-542.
- 437 Kaspi, Y., Galanti, E., Hubbard, W. B., Stevenson, D. J., Bolton, S. J., Iess, L.,
 438 ... Wahl, S. M. (2018, March). Jupiter's atmospheric jet-streams extend
 439 thousands of kilometres deep. *Nature*, *555*, 223-226.
- 440 Kaspi, Y., Galanti, E., Showman, A. P., Stevenson, D. J., Guillot, T., Iess, L., &
 441 Bolton, S. J. (2020). Comparison of the deep atmospheric dynamics of Jupiter
 442 and Saturn in light of the Juno and Cassini gravity measurements. *Space Sci.*
 443 *Rev.*, *216*(5), 1-27.
- 444 Laraia, A. L., & Schneider, T. (2015). Superrotation in terrestrial atmospheres. *J.*
 445 *Atmos. Sci.*, *72*(11), 4281-4296.
- 446 Lee, S., & Kaspi, Y. (2021). Towards an understanding of the structure of Jupiter's
 447 atmosphere using the ammonia distribution and the Transformed Eulerian
 448 Mean theory. *J. Atmos. Sci.*, *78*(7), 2047-2056.
- 449 Lewis, S. R., Read, P. L., Conrath, B. J., Pearl, J. C., & Smith, M. D. (2007). As-
 450 similation of thermal emission spectrometer atmospheric data during the Mars
 451 Global Surveyor aerobraking period. *Icarus*, *192*(2), 327-347.
- 452 Li, C., Ingersoll, A., Bolton, S., Levin, S., Janssen, M., Atreya, S., ... Zhang, Z.
 453 (2020). The water abundance in Jupiter's equatorial zone. *Nature Astronomy*,
 454 *4*(6), 609-616.

- 455 Li, C., Ingersoll, A., Janssen, M., Levin, S., Bolton, S., Adumitroaie, V., . . .
 456 Williamson, R. (2017). The distribution of ammonia on Jupiter from a pre-
 457 liminary inversion of Juno microwave radiometer data. *Geophys. Res. Lett.*,
 458 *44*(11), 5317–5325.
- 459 Limaye, S. S. (2007). Venus atmospheric circulation: Known and unknown. *J. Geo-*
 460 *phys. Res. (Planets)*, *112*(E4).
- 461 Little, B., Anger, C. D., Ingersoll, A. P., Vasavada, A. R., Senske, D. A., Breneman,
 462 H. H., . . . Team, T. G. S. (1999). Galileo images of lightning on Jupiter.
 463 *Icarus*, *142*(2), 306–323.
- 464 Liu, J., Goldreich, P. M., & Stevenson, D. J. (2008, August). Constraints on deep-
 465 seated zonal winds inside Jupiter and Saturn. *Icarus*, *196*, 653–664.
- 466 Liu, J., & Schneider, T. (2010). Mechanisms of jet formation on the giant planets. *J.*
 467 *Atmos. Sci.*, *67*, 3652–3672.
- 468 Miesch, M. S., & Hindman, B. W. (2011). Gyroscopic pumping in the solar near-
 469 surface shear layer. *Astrophys. J.*, *743*(1), 79.
- 470 Oyafuso, F., Levin, S., Orton, G., Brown, S., Adumitroaie, V., Janssen, M., . . . S.,
 471 B. (2020). Angular dependence and spatial distribution of Jupiter’s centimeter-
 472 wave thermal emission from Juno’s microwave radiometer. *Earth Planet. Sci.*
 473 *Lett.*, *7*(11), e2020EA001254. doi: <https://doi.org/10.1029/2020EA001254>
- 474 Porco, C. C., West, R. A., McEwen, A., Del Genio, A. D., Ingersoll, A. P., Thomas,
 475 P., . . . Vasavada, A. R. (2003). Cassini imaging of Jupiter’s atmosphere,
 476 satellites and rings. *Science*, *299*, 1541–1547.
- 477 Potter, S. F., Vallis, G. K., & Mitchell, J. L. (2014). Spontaneous superrotation and
 478 the role of Kelvin waves in an idealized dry GCM. *J. Atmos. Sci.*, *71*(2), 596–
 479 614.
- 480 Read, P. L., Lewis, S. R., & Vallis, G. K. (2018). Atmospheric dynamics of terres-
 481 trial planets. *Handbook of Exoplanets*, *144*, 2537–2557.
- 482 Salyk, C., Ingersoll, A. P., Lorre, J., Vasavada, A., & Del Genio, A. D. (2006, De-
 483 cember). Interaction between eddies and mean flow in Jupiter’s atmosphere:
 484 Analysis of Cassini imaging data. *Icarus*, *185*, 430–442.
- 485 Schneider, T. (2006, May). The general circulation of the atmosphere. *Ann. Rev.*
 486 *Earth Plan. Sci.*, *34*, 655–688.
- 487 Schneider, T., & Liu, J. (2009). Formation of jets and equatorial superrotation on
 488 Jupiter. *J. Atmos. Sci.*, *66*, 579–601.
- 489 Showman, A. P., & de Pater, I. (2005, March). Dynamical implications of Jupiter’s
 490 tropospheric ammonia abundance. *Icarus*, *174*, 192–204.
- 491 Taylor, F. W., Atreya, S. K., Encrenaz, T. H., Hunten, D. M., Irwin, P. G., &
 492 Owen, T. C. (2004). Jupiter: the planet, satellites and magnetosphere. In
 493 (pp. 59–78). Cambridge University Press.
- 494 Tollefson, J., Wong, M. H., de Pater, I., Simon, A. A., Orton, G. S., Rogers, J. H.,
 495 . . . S., M. P. (2017). Changes in Jupiter’s zonal wind profile preceding and
 496 during the Juno mission. *Icarus*, *296*, 163–178.
- 497 Vallis, G. K. (2017). *Atmospheric and Oceanic Fluid Dynamics* (second ed.).
 498 pp. 770. Cambridge University Press.
- 499 Vasavada, A. R., & Showman, A. P. (2005, August). Jovian atmospheric dynamics:
 500 An update after Galileo and Cassini. *Reports of Progress in Physics*, *68*, 1935–
 501 1996.
- 502 Wicht, J., & Gastine, T. (2020). Numerical simulations help revealing the dynamics
 503 underneath the clouds of Jupiter. *Nature Communications*, *11*(1), 1–4.
- 504 Wicht, J., Gastine, T., Duarte, L. D., & Dietrich, W. (2019). Dynamo action of the
 505 zonal winds in Jupiter. *Astron. and Astrophys.*, *629*, A125.
- 506 Young, R. M., & Read, P. L. (2017). Forward and inverse kinetic energy cascades in
 507 Jupiter’s turbulent weather layer. *Nature Physics*, *13*(11), 1135–1140.
- 508 Young, R. M., Read, P. L., & Wang, Y. (2019). Simulating Jupiter’s weather layer.
 509 Part I: Jet spin-up in a dry atmosphere. *Icarus*, *326*, 225–252.

Figure 1.

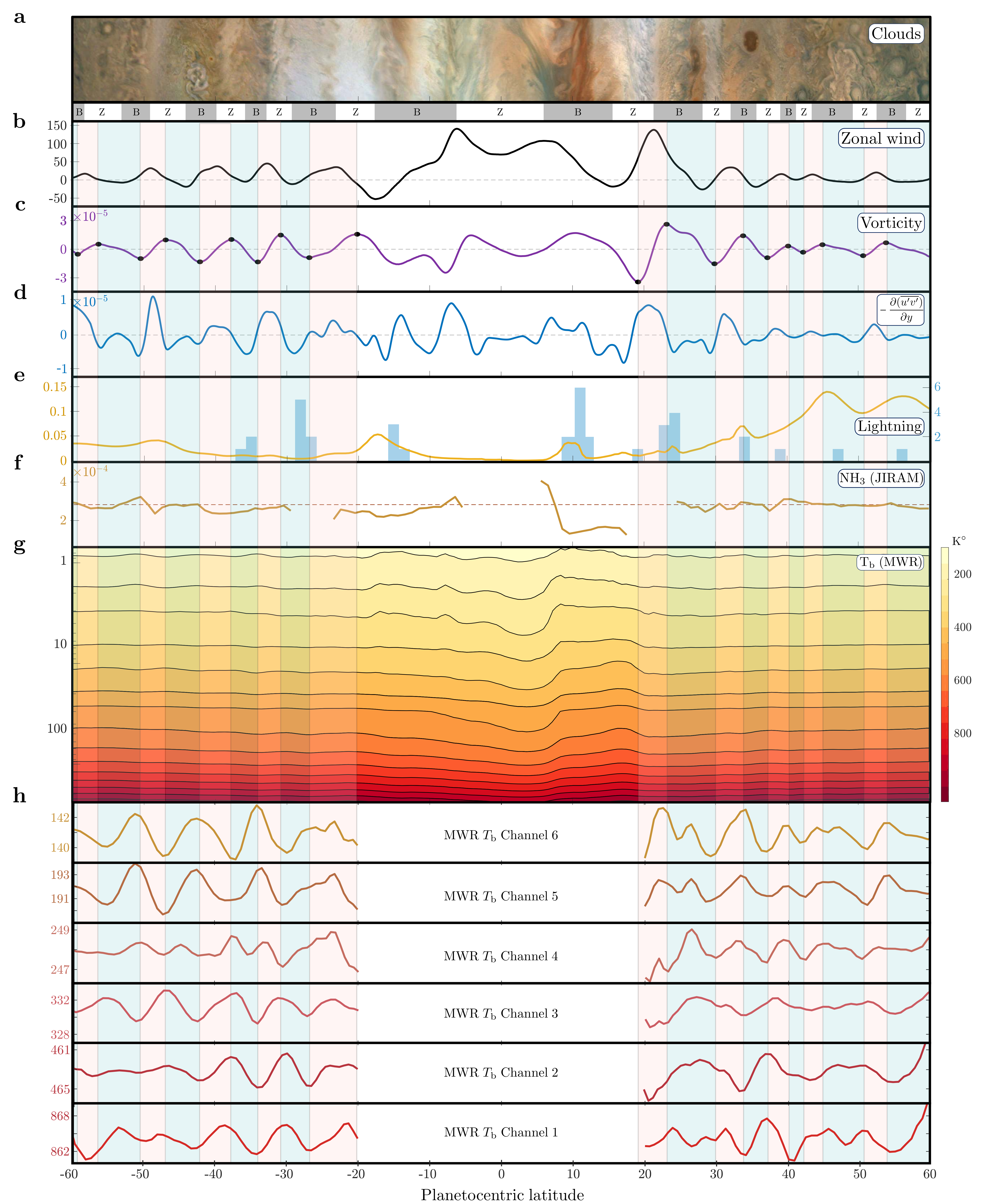


Figure 2.

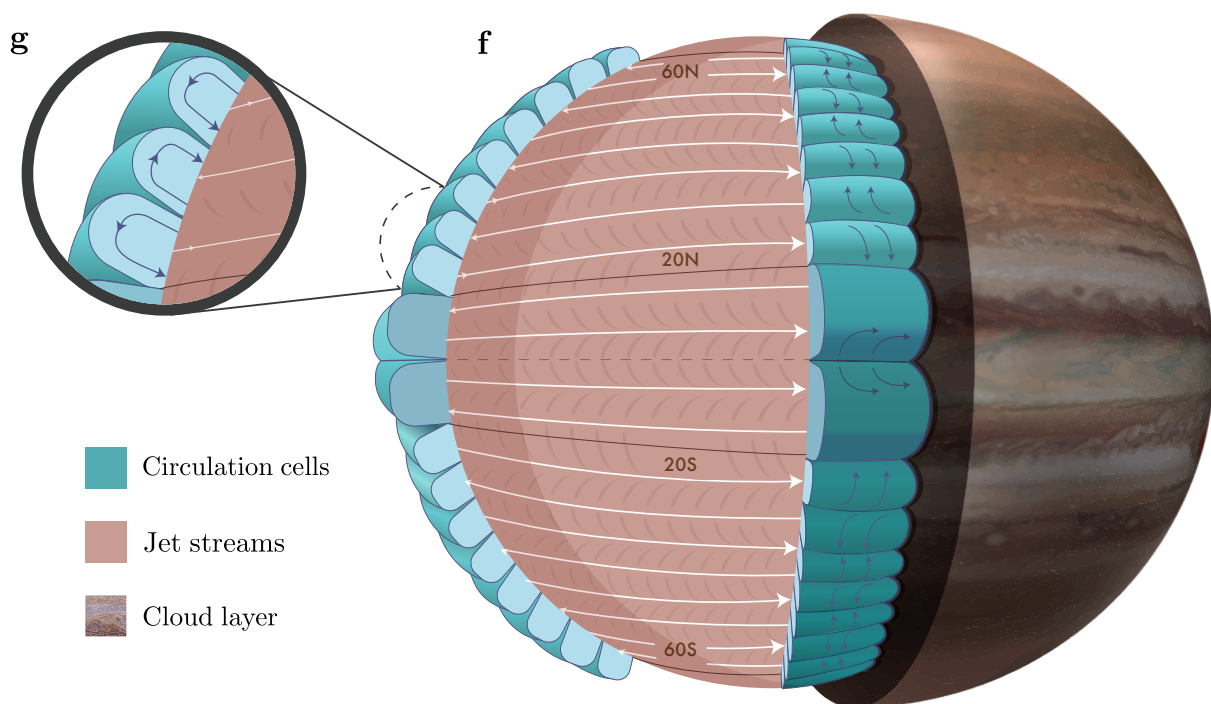
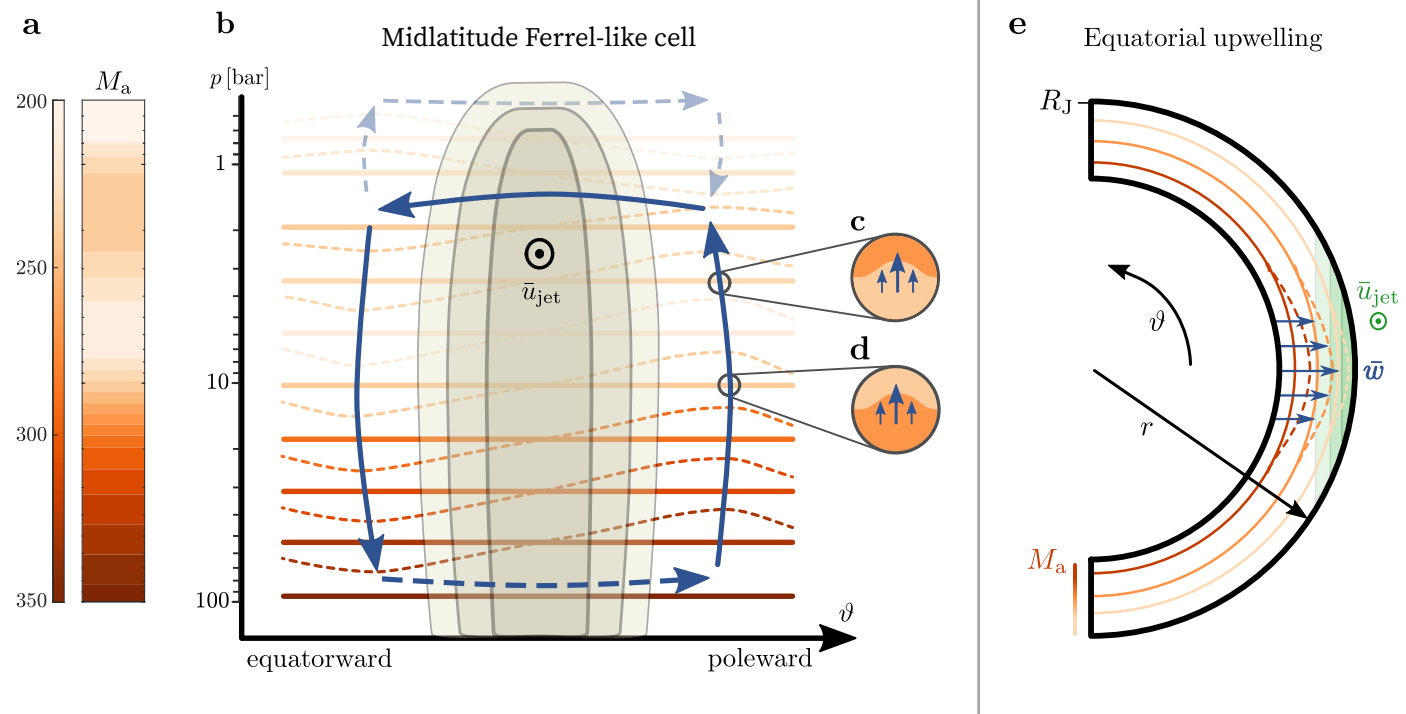


Figure 3.

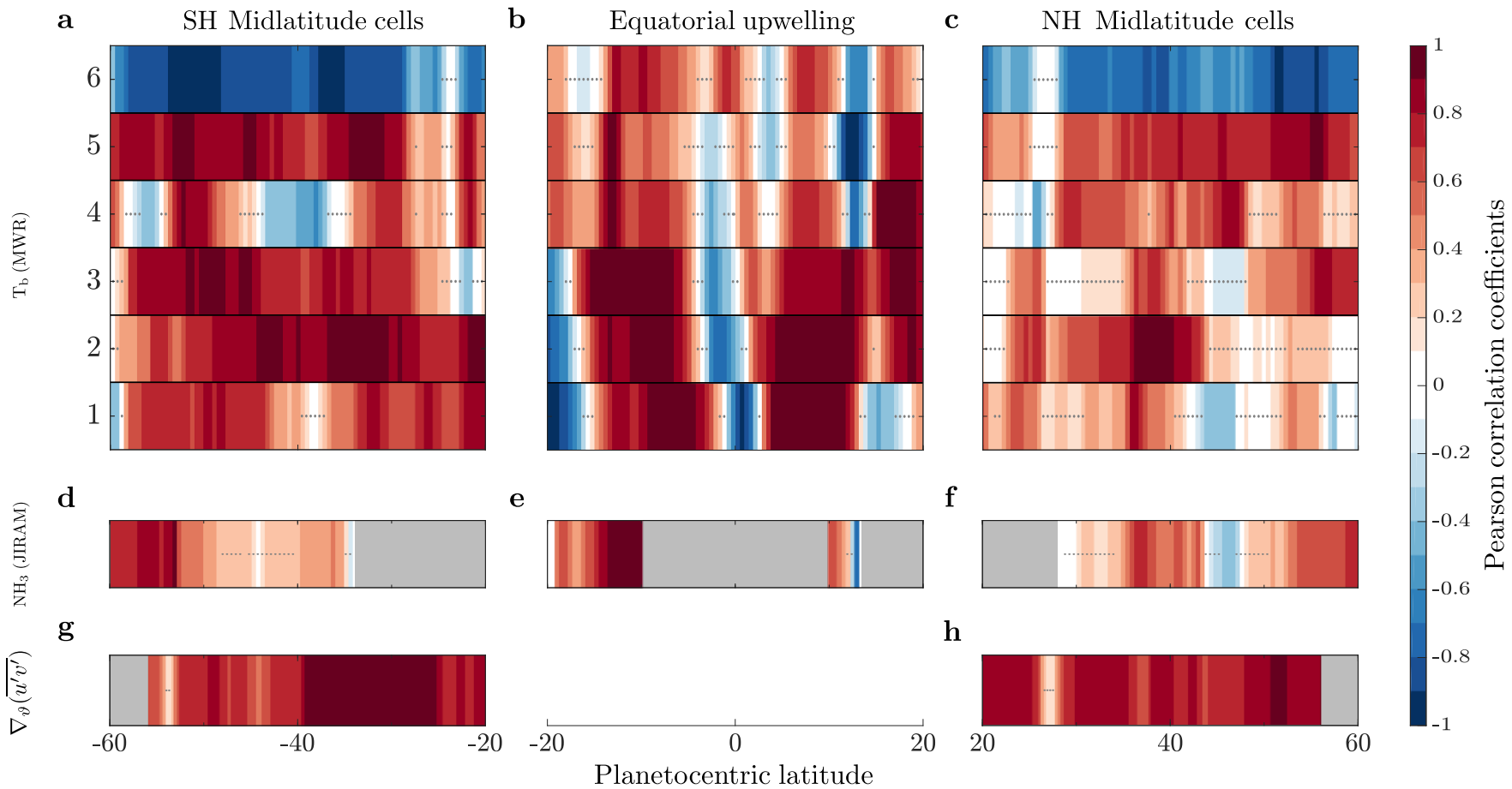


Figure 4.

